7
In Vitro and *In Silico* Based Mechanistic View of Therapeutic Antimicrobial Potential of Formazanate Based Mercury(II) Complex

Research Article based on this study:

Birara, S., Yadav, V. K, Jena A. K, Bhattacharyya, S., Metre, R. K. In Vitro and In Silico Based Mechanistic View of Therapeutic Antimicrobial Potential of Formazanate Based Mercury(II) Complex. ChemPlusChem, 2025, 90, e202400696.

7.1 Introduction

The pressing need for increased research in the development of innovative antimicrobial agents has been underscored by the ongoing antibiotic resistance crisis, marking the advent of the antimicrobial resistance (AMR) era [Abraham, 1963]. The speed at which clinically important pathogens are becoming resistant to current antimicrobial treatments is exceeding the pace at which new antimicrobial drugs are being introduced to the market [Abraham, 1963]. Decades-long uncontrolled clinical usage of antibiotics, as well as the indiscriminate usage of antibiotics in food and fodder industries, has culminated in the worldwide emergence of antibiotic-resistant traits amongst life-threatening human pathogens. Around the globe, new therapeutic leads are urgently needed to combat the imminent threat of antibiotic resistance. Multidrug-resistant bacterial infections are the major cause of worldwide mortalities and morbidities. According to a report published in 2019, 7.7 million deaths worldwide were accounted for in a single year due to major bacterial infections, which is the second largest cause of mortality compared to the cases reported with heart diseases [Ikuta et al., 2022; Vos et al., 2020]. Amongst the widely encountered bacterial pathogens, 33 were found to cause major infections. Out of that, more than half of the infections were predominantly caused by five bacterial species, which include *Escherichia coli*, *Staphylococcus aureus*, *Klebsiella pneumoniae*, *Streptococcus pneumoniae,* and *Pseudomonasaeruginosa* [Ikuta et al., 2022; Maglangit et al., 2021]. Hence, new antibacterial therapeutic leads are globally sought to treat infections caused by these predominant bacterial pathogens.

Metal and metal-complexes antimicrobials represent a promising avenue in the efforts to tackle antimicrobial resistance (AMR) [Lemire et al., 2013; Sovari & Zobi, 2020]. Certainly, the complexation of metals with ligands represents a strategy to enhance the medicinal properties of certain compounds. For instance, vanadyl-curcumin and copper-curcumin complexes exhibit greater therapeutic efficacy compared to curcumin in their isolated form [Prasad et al., 2021]. Investigations have substantiated the importance of inorganic elements in biological processes, given that many organic compounds utilized in medicine do not operate through purely organic means but rather engage with or undergo transformation facilitated by metal ions [Parmar et al., 2010]. Up until now, numerous metal complexes have undergone clinical trials for diagnostic and therapeutic purposes, showcasing a wide range of beneficial effects [Ndagi et al., 2017]. Lately,

there has been extensive research into the antimicrobial characteristics of Hg(II) complexes. Sabounchei et al. investigated the antibacterial effects of phosphorus ligands and their Hg(II) complexes, revealing that the Hg(II) complexes exhibited superior antibacterial activity compared to the unbound ligands against *Staphylococcus aureus* [Sabounchei et al., 2014]. The research by El-Megharbel and Refatrevealed that in contrast to Fe(III), Ag(I), and Cr(III) complexes, a Hg(II) clioquinol complex displayed the most significant activity against *Escherichia coli*, *Bacillus subtilis*, and *Aspergillus niger* [El-Megharbel & Refat, 2015]. Jahromi et al. discovered that coordinated Hg(II) complexes exhibited a more potent antimicrobial impact against all examined microorganisms (*S. aureus*, *B. subtilis*, *E. coli*, *Pseudomonas aeruginosa*, *Candida albicans*, and *A. niger*) compared to the tridentate ligand, leading to an approximately three-fold increase in the inhibition zone diameter [Mojahedi Jahromi et al., 2015]. In their research, Yousef et al. assessed the antibacterial activity of the (Z)-N-benzoyl-N'-(2-oxo-2-(phenylamino)acetyl)carbamothioic acid ligand and its metal complexes against *E. coli* and *B. subtilis*. Notably, the Hg(II) complex exhibited a slightly enhanced antibacterial effect compared to the ligand, as well as the Zn(II) and Cd(II) complexes.[Yousef et al., 2015] P.L. Lam et al. conducted a study in which they explored the prospective antimicrobial capabilities of a range of bis-(alkynyl)mercury(II) complexes containing bithiazole and oligothiophene linking components against *C. Albicans* and MRSA [Lam et al., 2016].

Among the several organic ligands, formazans and their modified molecular structures have garnered significant attention due to their remarkable pharmaceutical and therapeutic potentials as antitubercular [Raval et al., 2009], antihyperglycemic [Mahdi et al., 2015], antifertility [Kidwai et al., 1994], anticancer [Bhardwaj & Jolly, 1997], antioxidants [Bhosale et al., 2013], antibacterial [S. A. Khan et al., 2019; Mohammed & Dahham, 2018], anticonvulsant [Srivastava & Kumar, 2003], antiviral [Mukerjee et al., 1981], antiparkinsonian [Shawali & Samy, 2015c], anti-inflammatory [N. Singh et al., 2008], anti-HIV [Bhardwaj, 1998], analgesic [Kalsia et al., 1988], and antiproliferative agents. While there is a wealth of available reports concerning the utilization of formazans and their derivatives in biological applications, there is a notable shortage of reports focusing on formazan metal complexes in biological applications [S. A. Khan et al., 2020; Mariappan et al., 2010b]. Given the significant biological activities associated with formazan derivatives and Hg complexes, our study was formulated with the aim of synthesizing potent molecules for subsequent antibacterial activity. We opted to employ quinoline for substituting formazan because quinoline and its derivatives have been previously documented for their diverse range of biological activities, making them significant compounds in research [Behera et al., 2022; Insuasty et al., 2019].

In the present work, we introduce a newly synthesized [Hg^{II}(L3)Cl] complex (**6**) utilizing the formazan-based ligand, 3-Cyano-1,5-(quinolin-8-yl)formazan (L3H). To explore the antibacterial property of the synthesized [Hg^{II}(L3)Cl] complex, we performed the *in vitro* antibacterial assay followed by *in silico* identification of the plausible physiological target of the synthesized compound through a pharmacophore-guided rational drug designing approach. Notably, this complex has exhibited *in vitro* anti-bacterial activity against all four selected pathogens *E. coli*, *P. aeruginosa*, *B. subtilis,* and *S. aureus*. Moreover, through an *in silico* pharmacophore-guided drug discovery route, we have also outlined a plausible mechanism of action for the newly synthesized mercury complex. We found that this scaffold potentially interacts with one of the major DNA repair enzymes, AP endonuclease, that protects bacteria from dsDNA damage-induced cell death. The mechanistic detail of the mode of action of **6** against a broad range of bacterial pathogens is presented herein. The outcome herein would be highly useful in precisely targeting multiple drug-resistant bacteria, and this scaffold may serve as a potential broad-range antimicrobial therapeutic lead in the future.

7.2 Experimental Section

7.2.1 General Considerations

The ligand 3-Cyano-1,5-(quinolin-8-yl)formazan (L3H) was prepared by following the modified version of the reported method [Bxjdesinsky & Svec, 1971b]. All the solvents and chemicals used in this work were procured commercially, maintained at room temperature, and used as received without any further purification. In Chapter 2, detailed descriptions of the instruments used for various characterizations are provided.

7.2.2 Synthesis of 3-Cyano-1,5-(quinolin-8-yl)formazan [L3H]

In a solution consisting of 2-aminoquinoline (0.691 g, 4.8 mmol), 12 M concentrated hydrochloric acid (1.2 mL), and 15 mL of water, maintained at a temperature of -5 °C, sodium nitrite (0.38 g, 5.5 mmol) was added gradually in small portions over a duration of 5minutes. Following 20 minutes of stirring, the mixture was introduced into a second solution comprising cyanoacetic acid (0.21 g, 2.4 mmol), sodium hydroxide (0.96 g, 24 mmol), and 50 mL of water, all maintained at 0 °C. This addition was carried out over a 20-minute interval. After stirring for 16 hours, a black precipitate formed, which was filtered to produce a dark solid. The crude product was washed with distilled water, and methanol was further employed for its crystallization. Yield: 0.256 g (43%). ^{1}H NMR (500 MHz, $CDCl_3$): δ 13.89 (s, 1H), 8.93 (dd, J = 4.2, 1.7 Hz, 2H), 8.21 (dd, J = 8.3, 1.6 Hz, 2H), 7.93 – 7.86 (m, 2H), 7.61 (dd, J = 5.3, 4.4 Hz, 4H), 7.52 (dd, J = 8.3, 4.2 Hz, 2H) ppm.^{13}C NMR (126 MHz, $CDCl_3$): δ 150.35, 142.90, 141.17, 136.19, 128.83, 128.16, 127.50, 126.97, 122.14, 115.26, 114.90 ppm. FT-IR (KBr): 3041 (m), 2186 (m), 1632 (s), 1524 (m), 1492 (s), 1348 (s), 1281 (s), 1204 (m), 1046 (s), 817 (s), 781 (m) cm^{-1}. UV–vis ($CHCl_3$): λ_{max}322 nm (ε = 14,000 M^{-1} cm^{-1}), 466 nm (ε = 18,800 M^{-1} cm^{-1}). Exact mass calcd for $[C_{20}H_{13}N_7+H]^+$: 352.1304 Exact mass found: 352.1303.

7.2.3 Synthesis of [Hg^{II}(L3)Cl], 6.

Formazan L3H (35.1 mg, 0.1 mmol) was dissolved in 15 mL of methanol, followed by the addition of an equimolar amount of mercuric chloride (27.15 mg, 0.1 mmol); the mixture was allowed to reflux for 24 hours. Over the course of this period, a noticeable color change occurred, shifting from a dark red to a dark purple. The purple solid was separated via filtration and subjected to washes with both hexane and methanol. By slowly evaporating the concentrated DCM solution of the solid obtained, single crystals appropriate for X-ray analysis were grown. Yield: 30 mg (51%). ^{1}H NMR (500 MHz, $CDCl_3$) δ 8.92 (s, 2H), 8.35 (t, J = 7.3 Hz, 4H), 7.80 (d, J = 8.0 Hz, 2H), 7.69 (dd, J = 10.1, 5.7 Hz, 4H) ppm. FT-IR (KBr): 2213 (m), 1564 (m), 1501 (s), 1281 (m), 1231 (s), 1132 (s), 1082 (s), 894 (m), 826 (s), 776 (s), 767 (m), 660 (m), 628 (m) cm^{-1}. UV–vis ($CHCl_3$): λ_{max} 346 nm (ε= 11,200 M^{-1} cm^{-1}), 569nm (ε = 22,400 M^{-1} cm^{-1}). Exact mass calcd for $[C_{20}H_{12}ClHgN_7+H]^+$: 588.0621 Exact mass found: 588.0610. Anal. Calcd. (%) for $C_{20}H_{12}ClHgN_7$: C, 40.96; H, 2.06; N, 16.72. Found: C, 41.182; H, 2.088; N, 16.38.

7.2.4 Determination of antibacterial activity and minimum inhibitory concentration

The antibacterial activity of the formazanate-based mercury(II) complex (**6**) was determined against four representative strains of Gram-positive (*Bacillus subtilis* and *Staphylococcus aureus*) and Gram-negative (*Escherichia coli* and *Pseudomonas aeruginosa*) bacterial class by a zone of inhibition assay on the LB agar plates.[Kirby-Bauer Disk Diffusion Susceptibility Test Protocol; 2009. Www.Atcc.Org, n.d.] In brief, bacterial culture of optical density 0.6 grown in LB broth was spread on an LB agar plate followed by incubation at 37°C for 30 min. Complex **6** at a final concentration of 30 mM (20 µl) dissolved in 100% DMSO was poured into a well created in the agar plate alongside 20 µl of 100% DMSO as a negative control in a separate well of the same LB agar plate. All the plates were again incubated at 37°C overnight. After overnight incubation at 37°C, the clear zone surrounding the well, representing the killing of bacteria as a function of radial diffusion of the complex **6** or the control (DMSO) solutions, was measured. The radius of

the zone of inhibition represents the extent of bactericidal activity for a given bacterial strain. Moreover, we have determined the Minimal Inhibitory Concentration (MIC) value of complex **6** for each targeted bacteria by serial dilution method in the 96 well plates.[Wiegand, I.; Hilpert, K.; Hancock, R. E. W. Agar, and Broth Dilution Methods to Determine the Minimal Inhibitory Concentration (MIC) of Antimicrobial Substances. Nat Protoc 2008, 3 (2), 163–175. , n.d.] 100 µl of LB broth was added in each well; in the first well, an equal volume of sterile LB broth was mixed with an equal volume of 4mM complex **6** (dissolved in 100% DMSO), and further, this process was repeated up to last well with two-fold serial dilutions in each step. Herein, the concentration of complex **6** was employed from 2 mM to 3.9 µM along with negative control (with no bacteria) and positive control (with no ligand) for each bacterium. Similarly, an identical concentration of DMSO was also added in the separate set of wells to negate the background effect of DMSO on bacterial growth. 2 µl of log phase bacterial cultures were then added to each of the wells, followed by the incubation at 37°C overnight with no shaking. The MIC value was determined based on the observation of no growth of bacteria at the minimum concentration of complex **6** compared with the positive bacterial growth in corresponding negative control wells.

7.2.5 *In silico* pharmacophore-based therapeutic target screening of complex 6

Initially, the pharmacophore information of the synthesized complex **6** was obtained from its solved crystal structure. The obtained pharmacophore information was then used to screen plausible physiological targets of the compound through an *in silico* pharmacophore-based reverse docking approach using the therapeutic target database [Zhu et al., 2012]. Initial reverse docking results indicated AP endonuclease [Pidugu et al., 2023] could be a potential target of the synthesized ligand. To test the results obtained through the initial reverse docking approach further, Autodock vina, an application based on the Lamarkian Genetic Algorithm, was used to perform receptor-based molecular docking of **6** [Trott & Olson, 2010]. Crystal structure of *Bacillus subtilis* AP endonuclease (*Bs* AP endonuclease) and human AP endonuclease were downloaded from PDB (PDB ID: 5CFE and 5CFG, respectively) [Redrejo-Rodríguez et al., 2016], water, ligands, and other non-bonded molecules were deleted by using PyMol.['Schrödinger, n.d.] Polar hydrogen and Kollman charges were added to the receptor protomer using molecular graphic laboratory tools (MGL Tools) [Morris et al., 2009]. The same tool was used for complex **6** preparation and to fix the number of rotatable bonds of the **6**. Blind docking of **6** was performed with *Bs* AP endonuclease and human AP endonuclease using grid box sizes of 52ÅX52ÅX52Å and 54ÅX56ÅX54Å respectively, with the grid spacing of 1 Å. Out of nine poses, the best pose of the **6** was considered as it has the minimum root mean square deviation (RMSD) and minimum free energy of binding ($\Delta G_{Binding}$). The interaction profile of the ligand with *Bs* and human AP endonuclease was analyzed using PyMol and LigPlot [Wallace et al., 1995]. Further, we were interested in calculating the affinity of complex **6** with both the AP endonuclease enzymes. We have employed a deep learning-based online web server for affinity predictions [Jiménez et al., 2018].

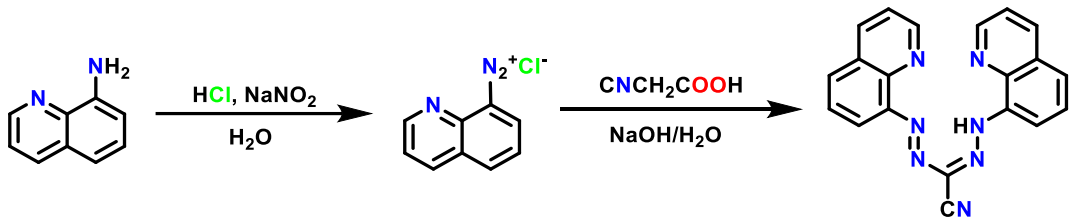
7.3 Results and Discussion

7.3.1 Synthetic Aspects

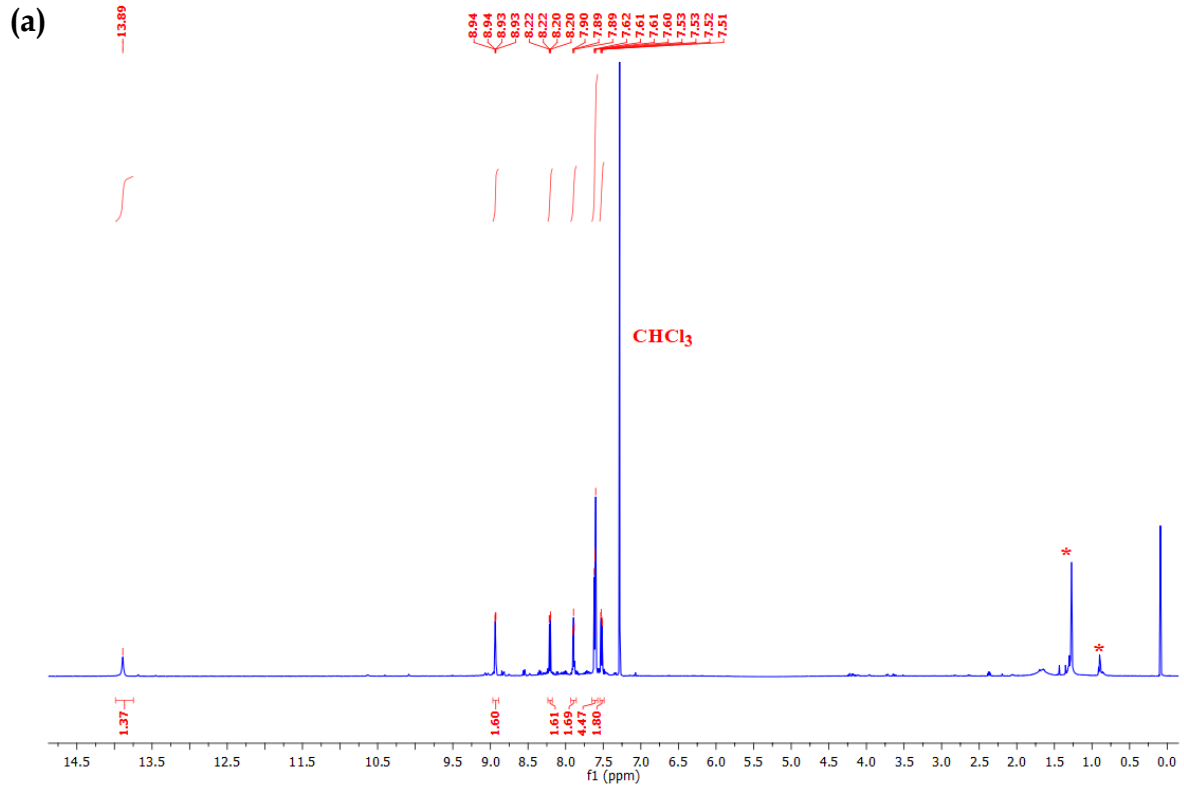
Scheme 7.1 illustrates the most frequently used method for preparing cyanoformazans. In an aqueous solution, an acidic methylene molecule, such as cyanoacetic acid, is deprotonated and reacted with aryldiazonium salts to generate formazan with a cyano group in the third position [Birara, Saini, et al., 2023]. By employing this approach, we have synthesized quinoline-substituted 3-cyanoformazan L3H, which has been previously documented but not fully characterized [Bxjdesinsky & Svec, 1971b]. The formation of ligand L3H was confirmed using ^{1}H and ^{13}C NMR spectroscopy (Figure 7.1), revealing characteristic formazan NH resonance in the ^{1}H NMR spectra at δ = 13.89 ppm, whereas the peaks at δ = 7.51–8.94 ppm are due to the aromatic protons of quinoline moieties. Further characterization of the ligand involves using various

analytical techniques such as FTIR, UV-Vis spectroscopy, and HRMS spectrometry. The HRMS analysis conducted in CH_3CN for L3H (Figure 7.2(a)) revealed a signal at 352.1303, indicative of the m/z value of the protonated parent organic ligand HL3, $[L3H+H]^+$, signifying its stability in the solution state. The FTIR spectrum of formazan L3H reveals the presence of intramolecular hydrogen bonding, as evidenced by the observation of a weak N-H band at 3041 cm^{-1}. The FT-IR spectra of LH exhibited a peak at 2186 cm^{-1}, which unequivocally verified the existence of the CN functional group [Birara, Saini, et al., 2023]. The presence of a peak at 1492 cm^{-1} in the L3H spectrum indicates the presence of the –N=N– group, which is consistent with the FTIR values reported earlier (Figure 7.2(b)) [Birara, Betal, et al., 2023d;].

The ligand (L3H) was employed to synthesize a mercury(II) complex, namely, [Hg(L3)Cl] (**6**). The ligand (LH) was treated with $HgCl_2$ in a methanolic solution under reflux conditions for 24 hours to produce complex **6**. The complex was isolated as a purple precipitate from its parent solution. The reaction pathway for synthesizing complex **6** is outlined in Scheme 7.2. The structure of complex **6** was comprehensively determined using a single-crystal X-ray diffraction technique and a combination of other analytical techniques, including ^1H NMR spectroscopy, UV-Vis spectroscopy, FTIR spectroscopy, thermogravimetric analysis, high-resolution mass spectrometry, and elemental analysis.



Scheme 7.1. Synthesis of benzothiazole-substituted formazan, L3H.



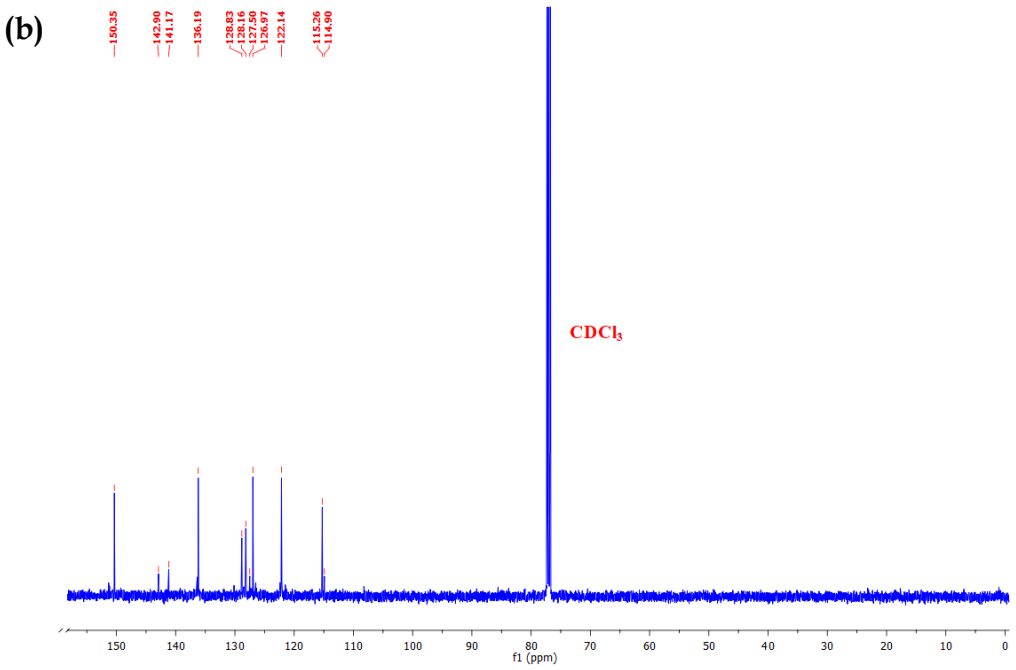


Figure 7.1. (a) ^{1}H NMR (500 MHz, $CDCl_3$) (b) ^{13}C NMR (126 MHz, $CDCl_3$) of L3H.

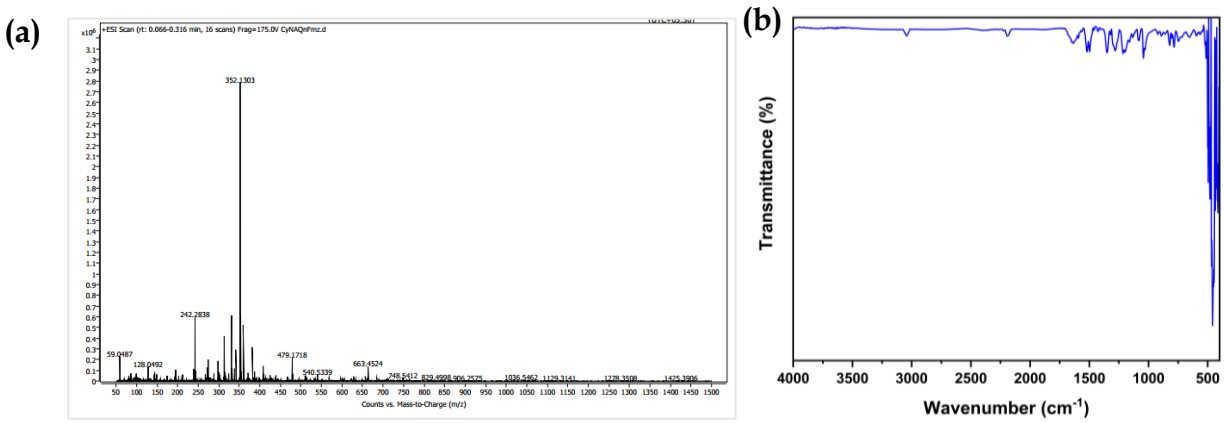
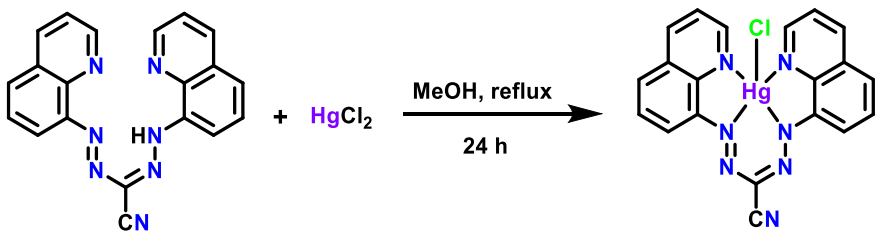


Figure 7.2. (a) HRMS analysis for L3H: Exact mass calcd for $[C_{20}H_{13}N_7+H]^+$: 352.1304 Exactmass found: 352.1303. (b) FT-IR spectrum of L3H

The signal at δ = 13.89 ppm from the internal free NH proton of the ligand LH disappeared after Hg^{+2} chelation, as shown in the ^{1}H NMR spectrum of **6** (Figure 7.3). Due to the low solubility of compound **6** in $CDCl_3$, ^{13}C measurement was not possible. The absence of the band at 3041 cm^{-1} in the FT-IR spectra of complex **6** suggests the loss of the NH proton, which was present in the L3H (Figure 7.4(b)). HRMS analysis shows a peak at m/z= 588.061 amu, which is due to $[Hg^{II}(L3)Cl+H]^+$, indicating that the complex is stable in solution (Figure 7.4(a)). The thermal stability of **6** up to 207°C (Figure 7.4(c)) was confirmed with thermogravimetric analysis (TGA).



Scheme 7.2. Synthesis of $[Hg^{II}(L3)Cl]$, **6**.

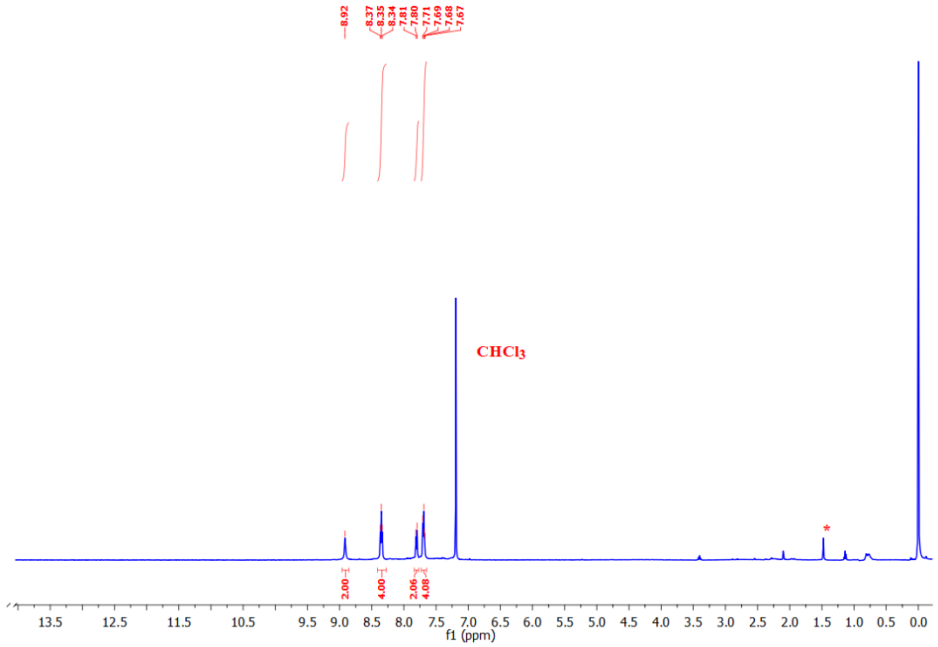


Figure 7.3. ^{1}H NMR (500 MHz, $CDCl_3$) of complex **6.**

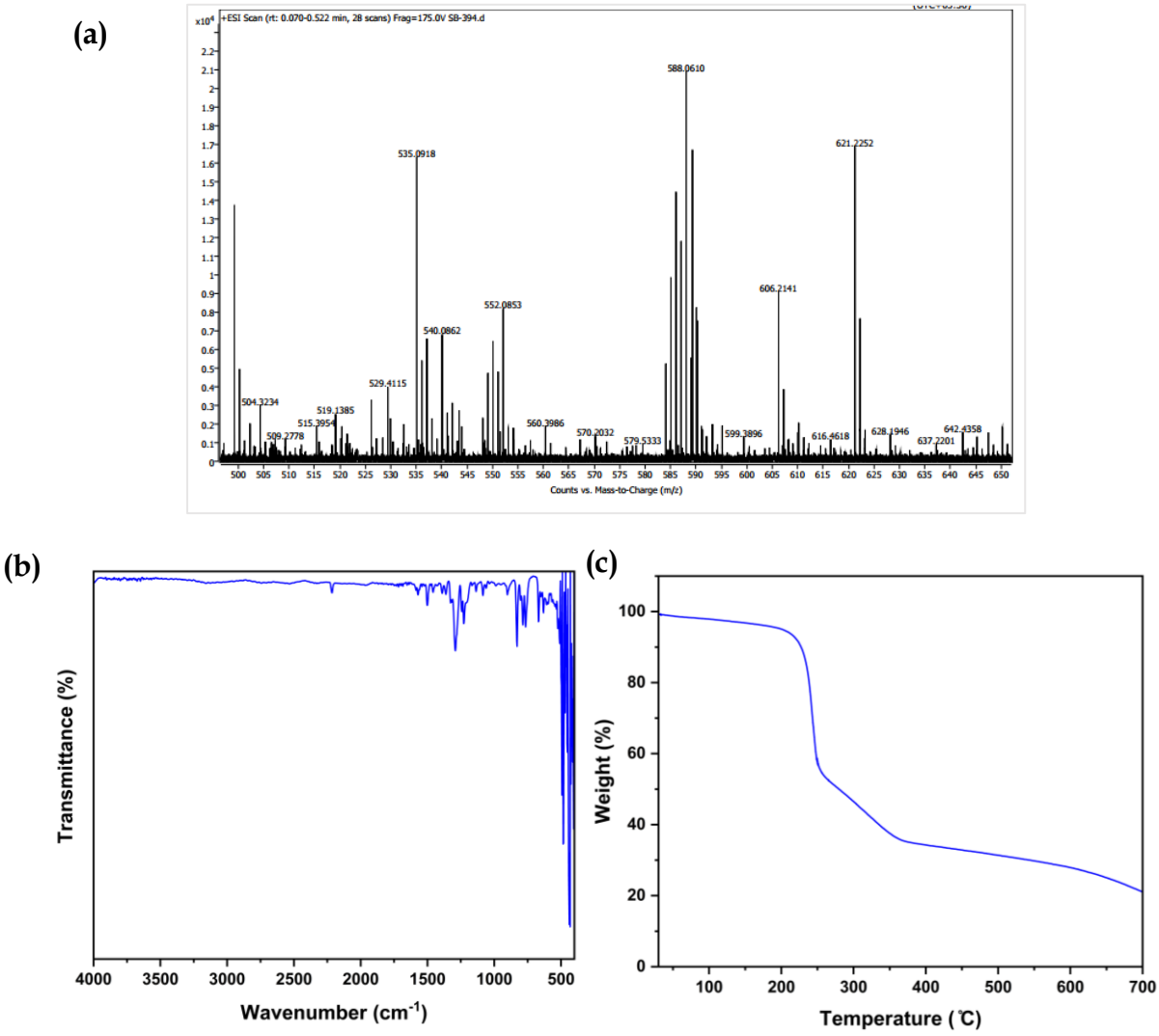
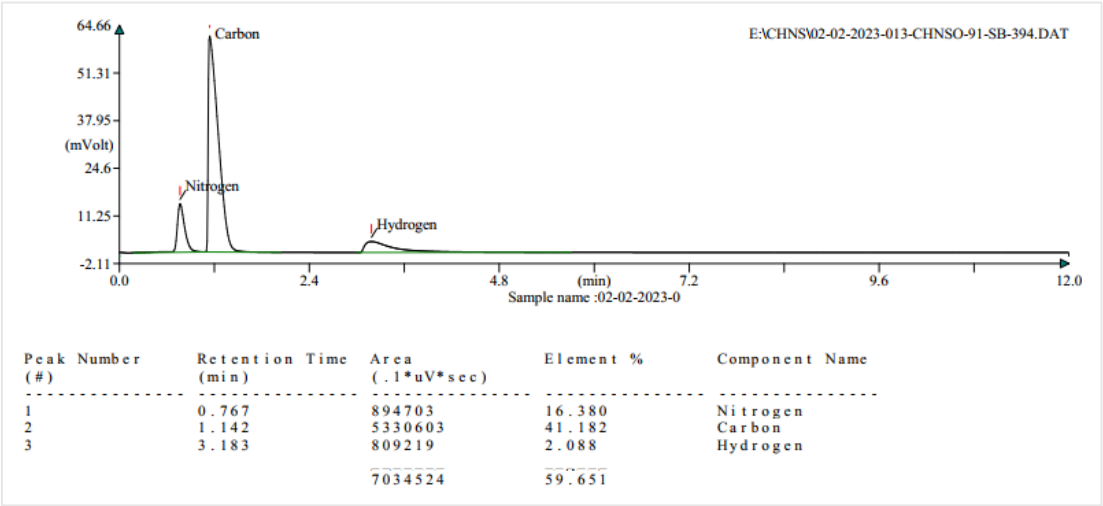


Figure 7.4. (a) HRMS analysis for **6**: Exact mass calcd for $[C_{20}H_{12}ClHgN_7+H]^+$: 588.0621 Exact mass found: 588.0610 (b) FT-IR spectrum of complex **6** (c) Thermogravimetric analysis of **6.**



Peak Number (#)	Retention Time (min)	Area (.1*uV*sec)	Element %	Component Name
1	0.767	894703	16.380	Nitrogen
2	1.142	5330603	41.182	Carbon
3	3.183	809219	2.088	Hydrogen
		7034524	59.651	

Figure 7.5. Elemental analysis of **6.** Anal. Calcd. (%) for $C_{20}H_{12}ClHgN_7$: C, 40.96; H, 2.06; N, 16.72. Found: C, 41.182; H, 2.088; N, 16.38.

7.3.2 X-Ray Crystallography

The molecular structure of complex **6** reveals that it belongs to the monoclinic system and the $P2_1/c$ space group. Figures 7.6(a) and 7.6(b) show the perspective and side view of the molecular structure of **6**, respectively. Table 7.2 contains the refinement parameters for the crystal structure of complex **6**. A summary of the selected bond and angle parameters associated with compound **6** is provided in Table 7.1.

The analysis of the single-crystal X-ray structure has revealed that **6** is a mono(formazanate)mercury complex, in which the Hg(II) center is bound to a tetradentate formazanate ligand, and the coordination sphere is completed by the incorporation of a chloride ligand, leading to the formation of a five-coordinate Hg(II) complex. The Hg center exhibits a notable displacement from the plane defined by the formazanate NNNN backbone, with a displacement of 0.812 Å from the N1-N4 plane. The relative co-planarity of the ligand backbone and N_4 binding pocket is significantly influenced by the size of the Hg atom. The geometry surrounding the Hg center can be most accurately described as a distorted square pyramidal (τ = 0.0706)[Trans et al., 1984] where the apical position is occupied by a Cl atom, and the basal plane is formed by the N_4 donors from deprotonated formazanate ligand, $L3^-$. The larger van der Waals radius of Hg(II) is probably responsible for both the increased N6-Hg-N7 bond angle observed in complex **6** [111.50(8)°] and the deviation [327.92°] from a total bond angle of 360° around the square plane formed by the Hg(II) within the N_4 pocket. The electron density within the π system of the chelate ring is delocalized, causing the N-N and C-N bond lengths to fall in the range between the typical single and double bond lengths for the respective atoms involved.

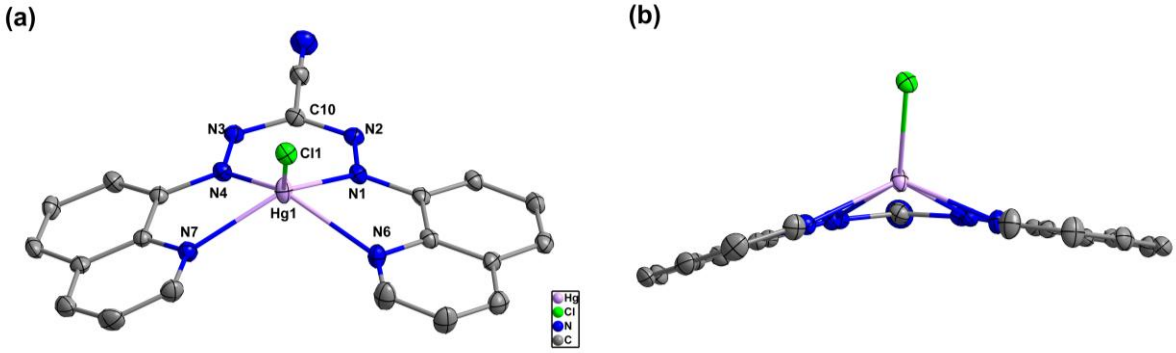


Figure 7.6. Molecular structure of **6:** (a) top view and (b) side view. Thermal ellipsoids are shown at the 50% probability level. Hydrogen atoms have been removed for clarity.

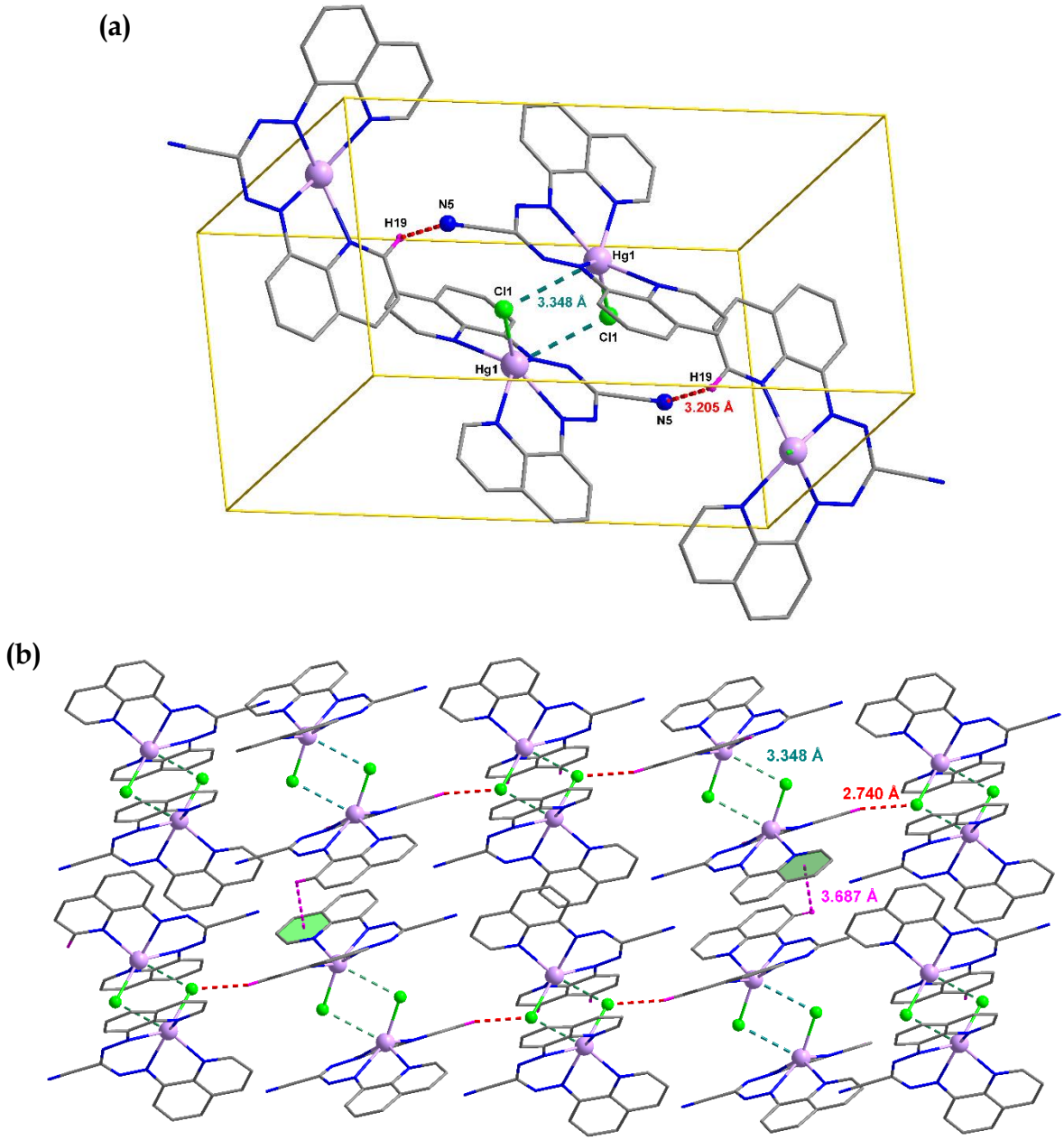


Figure 7.7. (a) C-H···N and Hg-Cl···Hg interactions in the unit cell of complex **6**. Bond distances (Å): C19-H19···N5, 3.205(33); Hg1-Cl1···Hg1, 3.348(7). Bond angles (deg): C19-H19-N5, 80.774(200); Hg1-Cl1-Hg1, 101.517(22). (b) C-H···Cl, Hg-Cl···Hg, and CH···π interactions in crystal packing of complex 1. Bond distances (Å): C18-H18···Cl1, 2.740(6); Hg1-Cl1···Hg1, 3.348(7); C7-H7···π, 3.687(1). Bond angles (deg): C18-H18-Cl1, 161.773(172); Hg1-Cl1-Hg1, 101.517(22).

Table 7.1. Selected Bond Angles (deg) and Selected Bond Distances (Å) for **6**.

6			
N1-N2	1.291(3)	N3-N4	1.300 (3)
N2-C10	1.349 (3)	N3-C10	1.350 (3)
Hg1-N1	2.348 (2)	Hg1-N4	2.318 (2)
Hg1-N6	2.403 (2)	Hg1-N7	2.371 (2)
Hg1-Cl1	2.443 (6)		
N1–Hg1–N6	70.28 (7)	N7–Hg1–N4	71.43 (7)
N4–Hg1–N1 N1–Hg1–N7	74.71 (7) 133.13 (8)	N6–Hg1–N7 N4–Hg1–N6	111.50 (8) 131.81 (8)
N6–Hg1–Cl1	90.79 (6)	N1–Hg1–Cl1	129.64(6)
N4–Hg1–C	137.37 (6)	N7–Hg1–Cl1	97.12 (6)

Table 7.2. Crystal data and structure refinement for **6** (CCDC2338966).

Identification code	6
Empirical formula	$C_{20}H_{12}ClHgN_7$
Formula weight	586.41
Temperature/K	100
Crystal system	monoclinic
Space group	$P2_1/c$
a (Å)	10.8664(4)
b (Å)	9.5736(4)
c (Å)	17.9538(7)
α (°)	90
β (°)	98.3120(10)
γ (°)	90
Volume (Å³)	1848.12(13)
Z	4
ρ_{calc}g.cm^{-3}	2.108
μ, mm^{-1}	8.496
F(000)	1112.0
Crystal size (mm³)	0.1 × 0.1 × 0.1
Radiation	MoKα (λ = 0.71073)
2Θ range for data collection (°)	3.788 to 56.692
Index ranges	-13 ≤ h ≤ 14, -12 ≤ k ≤ 12, -23 ≤ l ≤ 23
Reflections collected	30770
Independent reflections	4612 [R_{int} = 0.0393, R_{sigma} = 0.0252]
Data/restraints/parameters	4612/0/262
Goodness-of-fit on F²	1.030
Final R indexes [I>=2σ (I)]	R_1 = 0.0187, wR_2 = 0.0408
Final R indexes [all data]	R_1 = 0.0233, wR_2 = 0.0422
Largest diff. peak/hole (e Å^{-3})	1.35/-0.93

The unit cell of **6** is composed of four molecules that engage in interactions through CH--N and Hg--Cl bonds (Figure 7.7(a)). The crystal structure of compound **6** reveals a particularly notable feature: the presence of intermolecular spodium bonds between Hg1 and coordinated Cl atoms of the opposite molecules, with a distance of 3.348(7) Å. The presence of spodium bonds results in the interconnection of two molecules, forming a dimer with Hg1--Hg1 separations of 4.522(4) Å. The crystal packing is additionally reinforced by CH···π and CH---Cl interactions occurring between adjacent molecules, giving rise to a supramolecular arrangement as shown in Figure 7.7(b).

7.3.3 UV–Vis Spectroscopy

The optical properties of the formazan ligand L3H and its mono(formazanate)mercury chloride complex (**6**) were investigated by recording UV−vis absorption spectra in chloroform solution (Figure 7.8). It is known that uncoordinated formazans exhibit intense colors, with the absorption wavelength maxima being contingent upon the conformation and substitution pattern of formazans. "Closed" formazans, for instance, typically manifest intense absorption maxima within the range of 450 to 550 nm, while formazans adopting the "open structure" tend to display blue-shifted absorption maxima.[Gilroy, Otieno, Ferguson, Mcdonald, et al., 2008] The formazan ligand L3H exhibits an intense absorption band in the visible spectrum at 466 nm, which is attributed to an LLCT (π→ π*) transition that predominantly engages the highest occupied

molecular orbital (HOMO) and the lowest unoccupied molecular orbital (LUMO) orbital. The λ_{max} experiences a gradual redshift, from 466 nm to 569 nm, as a consequence of the complexation of the ligand L3H with mercury. The observed redshift in the transition can be attributed to the combination of improved localization and conformational restrictions resulting from the process of coordination [Gilroy, Patrick, et al., 2008].

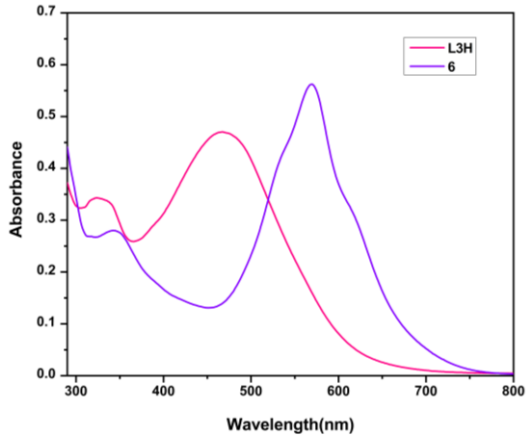


Figure 7.8. UV–vis spectra for formazan ligand L3H and compound **6** in $CHCl_3$ solution.

7.3.4 Cyclic Voltammetry

The electrochemical characteristics of **6** in DMF solution were examined using cyclic voltammetry utilizing a three-electrode cell setup and tetrabutylammonium hexafluorophosphate ($TBAPF_6$) as the supporting electrolyte. The cyclic voltammogram of complex **6**, as depicted in Figure 7.9, exhibits two quasi-reversible one-electron redox events at potentials of -0.89 V (ΔE= 88 mV) and -1.58 V (ΔE= 93 mV) relative to the Ag/AgCl reference electrode. The quasi-reversible peaks in the voltammogram correspond to the incremental reduction of the formazanate backbone, resulting in the generation of mono- and bis-radical anions of **6**. The reduction potentials observed for this complex align closely with the reported values for related compounds.[Jin et al., 2022b] Reversible reduction potentials of both peaks exhibited a notable difference (ΔE_{red}) of 690 mV.

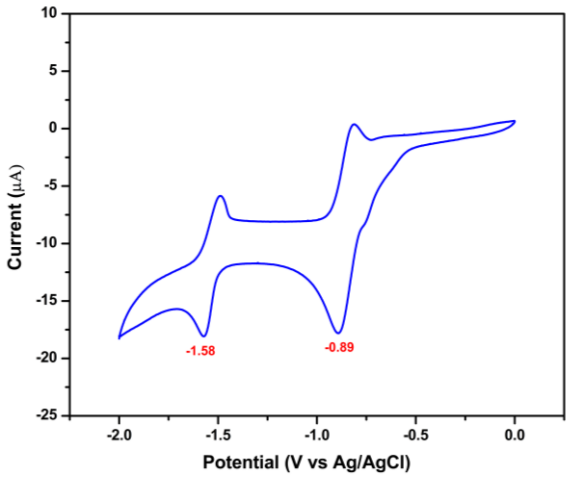


Figure 7.9. Cyclic voltammogram of **6** recorded at 10 mVs^{-1} in 1 mM DMF solution containing 0.1 M tetrabutylammonium hexafluorophosphate as a supporting electrolyte.

7.3.5 Evaluation of the Antibacterial Activity of 6

In order to test the broad-range antibacterial potential of the synthesized formazanate-based mercury(II) complex (**6**), we initially performed an agar plate antimicrobial disc diffusion assay.

We have chosen four bacterial genera, which will encompass Gram-positive (*Bacillus subtilis* and *Staphylococcus aureus*) and Gram-negative (*Escherichia coli* and *Pseudomonas aeruginosa*) bacterial pathogens. Our results (Figure 7.11A upper panel) indicate that synthesized [Hg^{II}(L3)Cl] complex (concentration: 30 mM dissolved in DMSO) can potentially kill all the four selected bacterial species as we can see a clear zone of inhibition of bacterial growth on the LB agar plate compared to the negative control (where only DMSO was used). The zone of inhibition diameter for respective bacterial species was found to be for *Bacillus subtilis*, ~1.2 cm; for *Staphylococcal aureus,* ~1.9 cm; for *Escherichia coli*, ~1.2 cm; and for *Pseudomonas aeruginosa*, ~1.1 cm. Intriguingly, in the case of *Escherichia coli*, a secondary zone of inhibition of about 2 cm in diameter with reduced bacterial growth (slightly opaque in appearance compared to a completely clear zone) has been obtained. This observation suggests that for *Escherichia coli*, complex **6** at lower concentrations may act as a bacteriostatic agent, whereas, at higher concentrations, the molecule is bactericidal. Furthermore, we have determined the minimum inhibitory concentrations (MIC) of the synthesized [Hg^{II}(L3)Cl] complex (**6**) against the aforementioned set of bacterial pathogens (Figure 5B upper panel). The MIC values for *B. subtilis*, *S. aureus*, *E. coli,* and *P. aeruginosa* were found to be 15.625 µM, 62.5 µM, 250 µM and 250 µM respectively. These results indicate that the bactericidal effect of **6** is approximately four times more effective against Gram-positive bacteria than Gram-negative ones. The presence of an outer membrane in the case of Gram-negative bacterial species with the complex lipidic composition of the lipopolysaccharide layer may account for lesser cell permeability and susceptibility towards the synthesized compound compared to the Gram-positive counterparts. We can corroborate that complex **6** is a broad-spectrum antibacterial agent, which is comparatively more effective against Gram-positive bacteria. The upper panel (A) represents the antibacterial activity test of **6** with disc diffusion assay against four indicated bacteria as the representatives of Gram-positive and Gram-negative classes. Figure B (upper panel) indicates the Minimal Inhibitory Concentration (MIC) determination against the same set of bacteria, along with the corresponding negative and positive controls. The table in Figure B represents the concentrations of complex **6** corresponding to the respective columns of a 96-well plate.

In the lower panel, the prediction of a plausible mechanism of action of **6** is represented using *in silico* approaches. Figure in the center (Lower panel) represents *Bacillus subtilis* AP endonuclease (PDB ID: 5CFE) docked with complex **6**, protein and complex **6** is aligned to human AP endonuclease (PDB ID: 5WN0 with RMSD of 0.550 Å) to demonstrate that **6** is binding near the metal binding site (5.2Å distance) and at the interface of protein-DNA interaction site of the catalytic groove. Figures **A** and **B** (lower panel) represent the 3D and 2D interaction profiles of the docked **6,** indicating conserved DNA binding residues of *Bs* AP endonuclease are involved in the interaction.

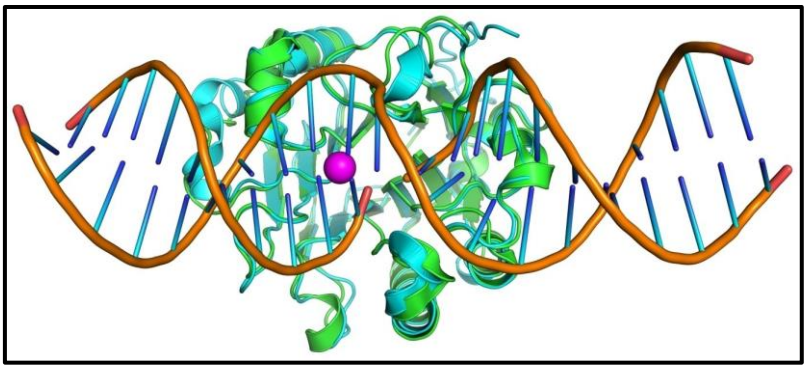


Figure 7.10. *Bacillus subtilis* AP endonuclease (PDB ID: 5CFE) overlapped with Human AP endonuclease DNA bound structure (PDB ID: 5DFI). *B. Subtilis* AP endonuclease is shown in green color that is bound with calcium at the active site (magenta color). Human AP endonuclease is shown in a cyan color that is DNA-bound. Both structures have a similar 3D organization with a very low alignment score (RMSD 0.550 Å).

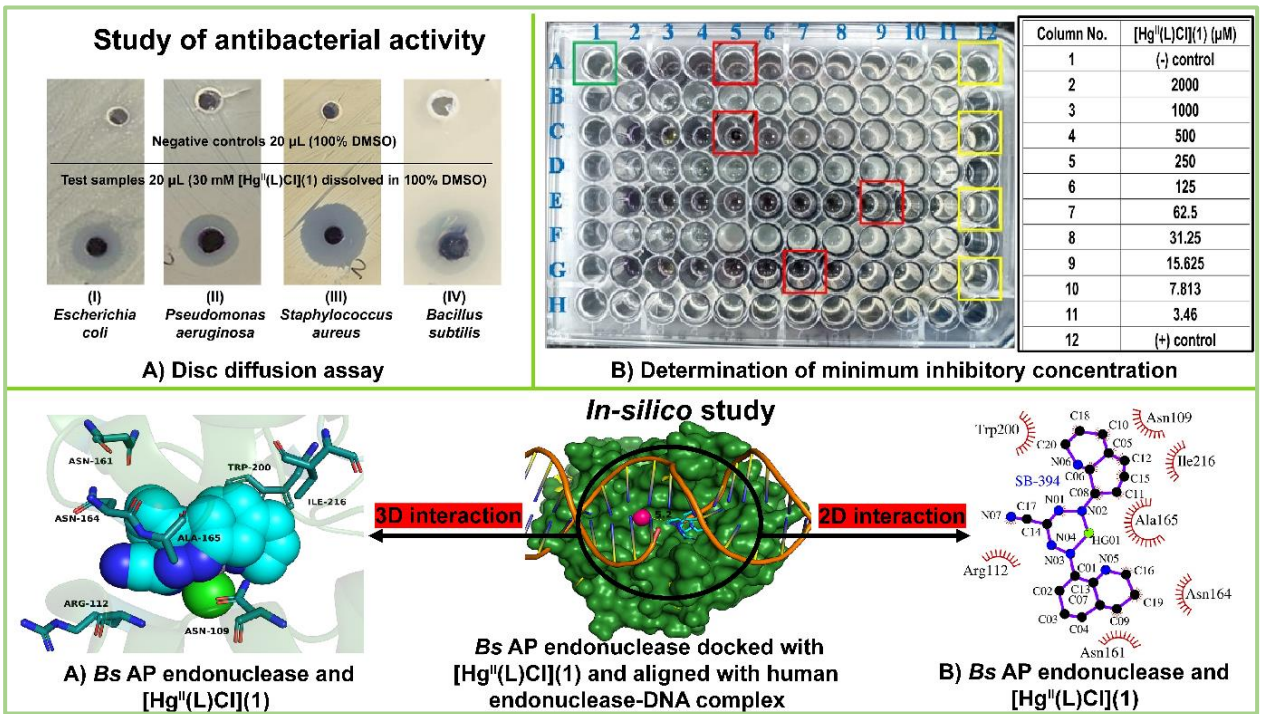


Figure 7.11. Antibacterial activity and plausible molecular mechanism of action of complex **6** as a function of binding at *Bacillus subtilis* AP endonuclease (*Bs* AP endonuclease) catalytic metal and dsDNA binding site (Active site).

In order to identify the plausible therapeutic target and to establish the molecular mechanism of bactericidal activity of **6**, we have applied a pharmacophore-guided drug-designing approach. The initial screening for plausible physiological targets indicates that AP endonuclease could be one of the potent targets of **6**. AP endonuclease is a ubiquitous enzyme obtained in both Gram-positive and Gram-negative bacteria and is involved in the dsDNA repair pathway [White & Allers, n.d.]. It is the major DNA repair enzyme that cleaves the phosphodiester bond of the DNA backbone at 5′ of apurinic/apyrimidinic sites and also exhibits 3′-5′ exonuclease activity [Chou & Cheng, 2002]. During the exponential growth of bacteria, producing oxidative free radicals through various metabolic pathways causes oxidative DNA damage, which, if not repaired in proper time, may lead to deleterious mutations, stalling of DNA replication, and finally, cell death. AP endonucleases are one of the essential enzymes that are actively involved in repairing oxidatively damaged dsDNA lesions; therefore, this enzyme is considered a pivotal anti-bacterial drug target [Onyango et al., 2011]. Similarly, in the case of cancer therapy, the anticancer effect of cancer therapeutic agents, like alkylating agents and radiation therapy, is ineffective because of human AP endonuclease (APE1). Hence, this indispensable enzyme is also considered a target for anticancer therapy [Pidugu et al., 2023]. There are multiple homologs of AP endonucleases exist throughout all genera, but AP endonuclease, including ExoA and endonuclease-IV, contributes major roles in DNA repair; hence, its inhibition is lethal for any cells, and it can be considered an attractive drug target for antibacterial and anticancer chemotherapy [Ibarra et al., 2008]. The major concern of targeting this enzyme is that it inhibits any AP endonuclease, so targeted drug delivery in desired tissue, cells, and bacteria needs to be employed to reduce adverse effects.

The subsequent detailed blind molecular docking studies indicate the synthesized [Hg^{II}(L3)Cl] complex, presented herein, selectively binds at the dsDNA binding interface in the active site catalytic cleft of *Bacillus subtilis* AP endonuclease (*Bs* AP endonuclease) and human AP endonuclease (Figure 7.10 down panel in center) with excellent profiles of free energy of binding ($\Delta G_{binding}$) -8.2 and -8.3 Kcal/Mol respectively (Table 7.4). We have performed the deep learning-based ligand binding affinity (pK_d) predictions of the tested complex **6** with human and *Bs* AP

endonuclease, and the results indicate that the ligand should bind with moderate affinity (pK_d values 5.07 and 4.93) to human and *Bs* AP endonuclease enzymes respectively.
Detailed amino acid interaction analysis of Bs AP endonuclease docked complex **6** reveals the participation of the active site amino acid residues (Figure 7.11A and 7.11B lower panel), which have been previously reported to be involved in binding and stabilization of incoming dsDNA molecules and subsequent cleavage of phosphodiester bonds at 5′ of AP site and phosphodiester bonds during 3′ -5′ exonuclease activity (active site amino acid residues of Bs AP endonuclease are listed in Table 7.3). Especially the amino acid residues, Asn109, Arg112, Asn161, Asn164, Ala165, and Trp200, which are involved in interaction with complex **6** (Figure 7.11B lower panel), are previously found to be involved either directly in the catalytic role of the enzyme or are essential for substrate DNA binding and stabilization at the catalytic cleft.[Whitaker et al., 2018] Therefore, binding of complex **6** with Bs AP endonuclease may inhibit the enzyme's apurinic site repair mechanism by competing with the binding and stabilization of the substrate DNA, which may further culminate in stalling of DNA replication to cell death. Overall, the results presented herein suggest that the synthesized formazanate-based mercury(II) complex shows a broad range of antibacterial activity, which may stem from its plausible inhibition of the essential dsDNA repair enzyme, AP nuclease of the target organism. Furthermore, the same chemical scaffold with an adequately targeted drug delivery mechanism may also serve as a potential anticancer agent against chemotherapeutic drug-resistant cancers. Detailed structure-function studies, along with pharmacokinetic profiling and toxicity studies, will ensure the safety of this scaffold for future therapeutic uses.

Table 7.3: Amino acid residues that constitute the active site of AP endonuclease: Since there is no DNA-bound structure of Bs AP endonuclease available, we have done the alignment with human AP endonuclease to find the residues involved in DNA interaction and catalytic activity. The corresponding amino acid residues in bacterial enzymes are listed here. The residue in red color (Bs AP endonuclease) indicates a mismatch from human AP endonuclease at the same position.

S.No.	Active site amino acid residues of AP endonuclease	
1	*Bacillus subtilis* (PDB ID: 5CFE)	Human (PDB ID: 5DFI)
2	Asn7	Asn68
3	Asn9	Asp70
4	Glu36	Glu96
5	Tyr63	Tyr128
6	Tyr106	Tyr171
7	Asn109	Asn174
8	Arg112	Arg177
9	Asp145	Asp210
10	Asn147	Asn212
11	Asn161	Asn226
12	Gly166	Gly231
13	Trp200	Phe266
14	Ser202	Thr268
15	Arg204	Met270
16	Trp214	Trp280
17	Asp242	Asp308
18	His243	His309

Table 7.4. *In silico* molecular docking and affinity prediction of complex **6** with AP endonuclease.

Sr. No.	Name of protein	Binding free energy Kcal/Mole	Affinity [pK_d($-\log K_d$)]
1.	Bs AP endonuclease	-8.2	4.93
2.	Human AP endonuclease	-8.3	5.07

7.4 Conclusion

The present work describes the synthetic pathway employed to produce a distorted square pyramidal mercury(II) complex using a cyanoformazan scaffold substituted with a quinoline moiety. Compound **6** demonstrated noteworthy electrochemical and optical characteristics. The CV data demonstrates the presence of reversible ligand-based redox chemistry in compound **6**, allowing for the formation of mono- and bis-radical anions. The investigation into the *in vitro* antibacterial activity of this complex demonstrated its enhanced efficacy against Gram-positive (*Bacillus subtilis* and *Staphylococcus aureus*) bacterial species compared to the Gram-negative (*Escherichia coli and Pseudomonas aeruginosa*) ones. The *in-silico* results corroborate its bactericidal mode of action via plausible inhibition of AP endonuclease activity, which is an essential enzyme involved in the repair of oxidatively damaged DNA. This work aims to establish a foundation for the systematic development of new Hg(II) compounds based on formazanate ligands, which have the potential to be utilized as broad-range anti-bacterial therapeutic leads in the future.